

4-22-2015

The Role of Bulge Formation in the Homogenization of Stellar Populations at $Z \sim 2$ as Revealed by Internal Color Dispersion in CANDELS

Steven Boada
Texas A&M University


V. Tilvi
Texas A&M University

R. F. Quadri
Texas A&M University

M. Hilton
University of Nottingham, UK

S. Finkelstein
University of Texas - Austin

See next page for additional authors

Follow this and additional works at: https://uknowledge.uky.edu/physastron_facpub
 [Click to open a feedback form in a new tab to let us know how this document benefits you.](#)
Part of the [Astrophysics and Astronomy Commons](#), and the [Physics Commons](#)

Repository Citation

Boada, Steven; Tilvi, V.; Quadri, R. F.; Hilton, M.; Finkelstein, S.; Guo, Yicheng; Bond, N.; Conselice, C.; Dekel, A.; Ferguson, H.; Gialalisco, M.; Grogin, N. A.; Kocevski, Dale D.; Koekemoer, A. M.; and Koo, D. C., "The Role of Bulge Formation in the Homogenization of Stellar Populations at $Z \sim 2$ as Revealed by Internal Color Dispersion in CANDELS" (2015). *Physics and Astronomy Faculty Publications*. 263.
https://uknowledge.uky.edu/physastron_facpub/263

Authors

Steven Boada, V. Tilvi, R. F. Quadri, M. Hilton, S. Finkelstein, Yicheng Guo, N. Bond, C. Conselice, A. Dekel, H. Ferguson, M. Giavalisco, N. A. Grogin, Dale D. Kocevski, A. M. Koekemoer, and D. C. Koo

The Role of Bulge Formation in the Homogenization of Stellar Populations at $Z \sim 2$ as Revealed by Internal Color Dispersion in CANDELS**Notes/Citation Information**

Published in *The Astrophysical Journal*, v. 803, no. 2, article 104, p. 1-14.

© 2015. The American Astronomical Society. All rights reserved.

Reproduced by permission of the AAS.

Digital Object Identifier (DOI)

<http://dx.doi.org/10.1088/0004-637X/803/2/104>

THE ROLE OF BULGE FORMATION IN THE HOMOGENIZATION OF STELLAR POPULATIONS AT $Z \sim 2$ AS REVEALED BY INTERNAL COLOR DISPERSION IN CANDELS

STEVEN BOADA¹, V. TILVI¹, C. PAPOVICH¹, R. F. QUADRI¹, M. HILTON^{2,3}, S. FINKELSTEIN⁴, YICHENG GUO⁸, N. BOND⁵, C. CONSELICE³, A. DEKEL¹⁰, H. FERGUSON⁶, M. GIAVALISCO⁷, N. A. GROGIN⁶, D. D. KOCEVSKI⁹, A. M. KOEKEMOER⁶, AND D. C. KOO⁸

¹ George P. and Cynthia Woods Mitchell Institute for Fundamental Physics and Astronomy, and Department of Physics and Astronomy, Texas A&M University, College Station, TX, 77843-4242, USA; boada@physics.tamu.edu

² Centre for Astronomy & Particle Theory, School of Physics and Astronomy, University of Nottingham, Nottingham, NG7 2RD, UK

³ Astrophysics & Cosmology Research Unit, School of Mathematics, Statistics and Computer Science, University of KwaZulu-Natal, Durban 4041, South Africa

⁴ Department of Astronomy, The University of Texas at Austin, Austin, TX 78712, USA

⁵ Laboratory for Observational Cosmology, Astrophysics Science Division, Code 665, Goddard Space Flight Center, Greenbelt, MD 20771, USA

⁶ Space Telescope Science Institute, 3700 San Martin Drive, Baltimore, MD 21218, USA

⁷ Department of Astronomy, University of Massachusetts, 710 North Pleasant Street, Amherst, MA 01003, USA

⁸ UCO/Lick Observatory and Department of Astronomy and Astrophysics, University of California, Santa Cruz, CA 95064, USA

⁹ Department of Physics and Astronomy, University of Kentucky, Lexington, KY 40506, USA

¹⁰ Center for Astrophysics and Planetary Science, Racah Institute of Physics, The Hebrew University, Jerusalem 91904, Israel

Received 2014 November 10; accepted 2015 February 20; published 2015 April 22

ABSTRACT

We use data from the Cosmic Assembly Near-infrared Deep Extragalactic Legacy Survey to study how the spatial variation in the stellar populations of galaxies relates to the formation of galaxies at $1.5 < z < 3.5$. We use the internal color dispersion (ICD), measured between the rest-frame UV and optical bands, which is sensitive to age (and dust attenuation) variations in stellar populations. The ICD shows a relation with the stellar masses and morphologies of the galaxies. Galaxies with the largest variation in their stellar populations as evidenced by high ICD have disk-dominated morphologies (with Sérsic indexes < 2) and stellar masses between $10 < \log(M/M_{\odot}) < 11$. There is a marked decrease in the ICD as the stellar mass and/or the Sérsic index increases. By studying the relations between the ICD and other galaxy properties including size, total color, star formation rate, and dust attenuation, we conclude that the largest variations in stellar populations occur in galaxies where the light from newly, high star-forming clumps contrasts older stellar disk populations. This phase reaches a peak for galaxies only with a specific stellar mass range, $10 < \log(M/M_{\odot}) < 11$, and prior to the formation of a substantial bulge/spheroid. In contrast, galaxies at higher or lower stellar masses and/or higher Sérsic index ($n > 2$) show reduced ICD values, implying a greater homogeneity of their stellar populations. This indicates that if a galaxy is to have a quiescent bulge along with a star-forming disk, typical of Hubble sequence galaxies, this is most common for stellar masses $10 < \log(M/M_{\odot}) < 11$ and when the bulge component remains relatively small ($n < 2$).

Key words: galaxies: evolution – galaxies: general – galaxies: stellar content – galaxies: structure

1. INTRODUCTION

In the local universe, galaxies separate into two broad classes (Kauffmann et al. 2003; Baldry et al. 2004): (i) large disk-dominated galaxies show ongoing star formation rates (SFRs) comparable to their past averages, as evidenced by their overall blue colors, and frequent spiral arms, and (ii) spheroidal, or bulge-dominated, galaxies with current SFRs much less than their past averages. However, especially in the more distant universe, there exists a third class of galaxies that exhibits a large amount of stellar population diversity and irregular morphologies (e.g., Giavalisco et al. 1996; Lowenthal et al. 1997; Dickinson 2000; Papovich et al. 2005). The mechanism by which a galaxy transitions from a uniformly blue, star-forming galaxy (with either disk-dominated or irregular morphologies) into a bulge-dominated, quiescent galaxy remains an open question.

Many studies have added to a growing body of evidence that the irregular morphologies are due, at least in part, to heterogeneous (clumpy) star formation (e.g., Elmegreen et al. 2005, 2008, 2009a, 2009b; Wuyts et al. 2011b, 2012, 2013; Guo et al. 2012, 2014; Adamo et al. 2013). Believed to be formed through gravitational instabilities in gas-rich disks

(e.g., Keres et al. 2005; Dekel & Birnboim 2006; Dekel et al. 2009a; Dekel & Burkert 2014), these clumps typically contribute 10%–20% of the total galaxy light (Förster Schreiber et al. 2011), and most have bluer colors and elevated specific star formation rates (sSFRs) compared to the surrounding regions (Guo et al. 2012, 2014). This contrast between a young star-forming region and the older underlying galaxy population may lead to a large amount of variation in the internal colors of a galaxy.

The ability to investigate the separation (heterogeneity) of the different stellar populations (blue star-forming clumps versus the older, redder stellar disk) becomes increasingly difficult at high redshift, because a galaxy’s morphology often depends heavily on the bandpass in which the galaxy is observed. For example, observed optical light (rest-frame UV) traces the distribution of unobscured star-forming regions (Dickinson 2000), which are often non-uniformly distributed.

Recent observations of clumpy galaxies (e.g., Guo et al. 2012, 2014; Wuyts et al. 2012, 2013; Adamo et al. 2013) find that clumps located toward galaxy centers are older and redder than clumps located toward the outskirts. This suggests that highly star-forming clumps may migrate toward the center where they could condense to form a classical

bulge (e.g., Ceverino et al. 2015). The formation of such a bulge, in turn, could be sufficient to stabilize the stellar disk against new star formation (Martig et al. 2009), homogenizing the stellar populations and reducing the variations in internal color. If this scenario is correct, we would expect to observe a relation between the internal color dispersion (ICD) of a galaxy and the formation of a bulge.

To investigate any potential relation, we require a tool to quantify the stellar population diversity of a galaxy. Traditional morphological classification methods—visual inspection, Sérsic profile fitting, concentration and asymmetry values (Conselice et al. 2004), and Gini coefficients (Lotz et al. 2004)—are calculated in a single bandpass and, as such, do not provide enough insight into the stellar population variations. Papovich et al. (2003) developed a differential morphological measure, the ICD, which quantifies the heterogeneity of stellar populations (such as with clumps) between bandpasses; galaxies with non-uniform distributions of young stellar populations give rise to a larger ICD than a galaxy with a homogeneous or evenly mixed stellar population. Similarly, galaxies with variable amounts of extinction will also exhibit large ICD values, due to the spatial variations in the reddening. Combining the ICD with other morphological indicators that quantify the distribution of light in a galaxy (e.g., Sérsic, Gini- M_{20} , concentration and asymmetry) provides insight into galaxies’ physical properties, such as clumpy star formation and their evolution in both overall color and structure.

In this paper, we build on previous studies (e.g., Papovich et al. 2003, 2005; Bond et al. 2011; Law et al. 2012), and we use the ICD as the primary metric in a comparative study of the rest-frame UV and optical morphological properties of the largest sample (>2500) of $1.5 < z < 3.5$ galaxies to date. In addition to broad IR coverage, we combine optical and near-infrared (near-IR) data from *Hubble Space Telescope* (*HST*) from the southern region of the Great Observatories Origins Deep Survey and Cosmic Assembly Near-infrared Deep Extragalactic Survey, which also includes the deeper data in the Hubble Ultra Deep Field (HUDF). We investigate the presence of heterogeneous stellar populations in a sample of $1.5 < z < 3.5$ galaxies and interpret our results in the context of galaxy evolution where a galaxy transitions from a disk-dominated to a more bulge-dominated morphology while experiencing a suppression of the diversity in its stellar populations.

In Section 2 we discuss the data and sample selection. We discuss the ICD measuring technique in detail in Section 3. We compare ICD and other galaxy properties in Section 4 and discuss possible causes of high ICD in Section 5. We discuss the role of star-forming clumps in galaxy evolution in Section 6 and summarize our results in Section 7.

Throughout this paper, we use a concordance cosmological model ($\Omega_{\Lambda} = 0.7$, $\Omega_m = 0.3$, and $H_0 = 70 \text{ km s}^{-1} \text{ Mpc}^{-1}$), assume a Chabrier initial mass function (IMF; Chabrier 2003), and use AB magnitudes (Oke 1974).

2. DATA

For this work, we make use of deep imaging data taken as part of the Cosmic Assembly Near-infrared Deep Extragalactic Survey (CANDELS; PIs Faber and Ferguson; Grogin et al. 2011; Koekemoer et al. 2011) of the southern region of the Great Observatories Origins Deep Survey (GOODS, hereafter referred to as GOODS-S; Giavalisco et al. 2004) along with

extremely deep observations of the HUDF. The large variation in depth between the GOODS-S observations and the HUDF ensures that we have access to galaxies with a large range in stellar mass.

We take advantage of the third version of the Advanced Camera for Surveys (ACS) mosaics in GOODS-S, which includes images taken with F435W, F606W, F775W, and F850LP (hereafter referred to as B_{435} , V_{606} , i_{775} , and z_{850}). In addition, we use imaging obtained from Wide Field Camera 3 (WFC3) in F098M, F105W, F125W, and F160W (hereafter as Y_{098} , Y_{105} , J_{125} , and H_{160}). The WFC3 imaging is split into two parts; the deep portion covers the central 50% of GOODS-S, with the wide portion covering the southern most 25% to a depth approximately 1 mag shallower than the deep portion. To complete our WFC3 coverage of GOODS-S, we make use of the WFC3 Science Organizing Committee’s Early Release Science program (PI O’Connell; Windhorst et al. 2011), which covers the northern 25% in Y_{098} , J_{125} , and H_{160} .

In addition, we include very deep imaging of the HUDF taken with both ACS (Beckwith et al. 2006) and WFC3 as part of HUDF 09 (PI Illingworth; e.g., Bouwens et al. 2010; Oesch et al. 2010) and UDF 12 (PI Ellis; Ellis et al. 2013). Both the ACS and WFC3 data sets contain imaging using the previously mentioned seven bandpasses.

2.1. Source Detection and Photometric Data

We use a multi-wavelength photometric catalog of the GOODS-S region provided by Guo et al. (2013). In this catalog, the sources are detected in a H_{160} mosaic drizzled to $0''.06 \text{ pixel}^{-1}$. Along with the source detections, photometry covering $0.4\text{--}8 \mu\text{m}$ (VIMOS U, B_{435} , V_{606} , i_{775} , z_{850} , Y_{098} , Y_{105} , J_{125} , H_{160} , ISSAC Ks, IRAC 3.6, 4.5, 5.8, and $8 \mu\text{m}$) is provided. The photometric data for the *HST* bands are computed by SExtractor (Bertin & Arnouts 1996) on images that have had their point-spread function (PSF) convolved to match the H_{160} resolution, while the lower-resolution ground-based and *Spitzer*/IRAC imaging is processed by TFIT (Laidler et al. 2006). See Guo et al. (2013) for full details on the construction of the photometric catalog.

2.2. Photometric Redshifts

We make use of the photometric redshifts for the galaxies in our sample derived by Dahlen et al. (2013). This photometric redshift catalog is constructed by combining redshifts derived by 11 different investigators using different photometric redshift codes, e.g., EAZY (Brammer et al. 2008), HyperZ (Bolzonella et al. 2000), LePhare (Arnouts et al. 1999; Ilbert et al. 2006), etc. These photometric redshift codes derive redshifts by fitting different combinations of spectral energy distribution templates and priors including available spectroscopic redshifts. We make use of spectroscopic redshifts where available (see Dahlen et al. 2013 for the compilation of spectroscopic data sets). The scatter between the photometric redshifts and corresponding spectroscopic redshifts, which span $z \sim 0\text{--}6$, is rms $[\Delta z / (1 + z_{\text{spec}})] = 0.03$, where $\Delta z = z_{\text{spec}} - z_{\text{phot}}$.

2.3. Sample Selection

Papovich et al. (2003) showed that galaxies with heterogeneous stellar populations have high ICD between their rest-frame UV and optical light. For our galaxy sample with

$1.5 < z < 3.5$, the CANDELS ACS and WFC3 bands probe rest-frame UV and optical wavelengths, respectively. Using the photometric redshifts described previously (Section 2.2), we select all galaxies with photometric or spectroscopic redshifts in this range. We apply a magnitude limit of 25 mag in H_{160} , which allows for a robust determination of morphological parameters and the ICD values (see Section 3.2 for reasoning). To avoid stars, we remove objects with stellarity index > 0.78 ; stellarity derived using `SExtractor` gives a likelihood of an object being a star. Applying this set of criteria yields a parent sample of 3369 galaxies.

2.4. Stellar Masses

Because the photometric redshifts are the result of the combination of the probability density functions from many routines, Dahlen et al. (2013) show they provide more accurate estimates of the redshift. The method employed by Dahlen et al. (2013) does not provide additional physical properties for the CANDELS galaxies. We derive stellar population parameters for the galaxies in our sample using FAST (Kriek et al. 2009), a stellar population synthesis modeling and fitting code. We fix the galaxy’s redshift at the photometric redshift from the Dahlen et al. (2013) catalog and fit 14-band galaxy photometry covering $0.4\text{--}8\ \mu\text{m}$ with model spectral energy distributions to estimate the stellar masses (along with dust attenuation) for the galaxies in the sample. We used models for a range of stellar population properties from the 2003 version of the Bruzual & Charlot (2003) stellar population synthesis models allowing for a range of attenuation ($A_v = 0\text{--}4$ mag) using the Calzetti et al. (2000) extinction law. We opt to use Bruzual & Charlot (2003) to facilitate the comparison to other studies and because recent work shows that the 2007 version of the Bruzual & Charlot (2003) models may overestimate the contributions of late-type giants to the near-IR (e.g., Zibetti et al. 2012). We assumed models with a delayed, exponentially declining ($\log \tau = 7\text{--}11$) star formation history, solar metallicity, and a Chabrier (2003) IMF.

Using a Salpeter IMF (Salpeter 1955) would to first order increase systematically the stellar masses by $\simeq 0.25$ dex. Using different assumptions for the stellar population metallicities will affect the derived stellar masses by $\simeq 0.2$ dex (Papovich et al. 2001). The average uncertainty in stellar mass for our sample is 0.11 dex, although errors from systematics in the metallicities, star formation histories, and other aspects of the spectral energy distribution fitting likely dominate (e.g., Kriek et al. 2009; Papovich et al. 2014).

The errors on the photometric redshifts do not influence greatly our conclusions. While photometric error uncertainties can affect the derivation of stellar population parameters, for small photometric redshift errors, like those for our sample, the contribution to the stellar mass uncertainty is minimal because small changes in redshift translate to small changes in distance (see discussion in Dickinson et al. 2003). For example, our uncertainty of rms $[\Delta z/(1+z)] = 0.03$ corresponds to a change in luminosity distance of $\sim 5\%$ for our sample. Because the stellar mass scales quadratically with luminosity distance, the mass uncertainty from photometric redshift errors is similarly small, $\sim 10\%$. This error is much smaller than systematic uncertainties in stellar mass arising from model fitting (see discussion in Papovich et al. 2014), and so we neglect errors from the photometric redshifts on the stellar masses.

Along with stellar masses, FAST provides an estimate of the total attenuation (A_v) due to dust in a galaxy. We use this value in Section 5.5 to understand better how the ICD might be affected by reddening due to dust.

2.5. Morphological Indicators

We use the structural catalog provided by van der Wel et al. (2012), which provides Sérsic index, n (Sérsic 1963), and the effective radius, R_e (measured along the major axis of the galaxy), for all sources in the GOODS-S catalog from Guo et al. (2013). These parameters are produced by GALFIT (Peng et al. 2002) using the best-fitting Sérsic models for the objects in the H_{160} imaging.

We also use the non-parametric indicators Gini parameter (G) and the second-order moment of the brightest 20% of the galaxy light, M_{20} . These indicators quantify the spatial distribution of light without assuming a specific functional form when classifying the morphologies of disturbed or irregular galaxies. For a complete description of this method see Lotz et al. (2004).

2.6. Color Gradients

We use color gradient measurements from M. Hilton et al. (2015, in preparation), where Hilton et al. compute the color gradients between the core and outskirts by centering annular apertures on each galaxy. They define concentric, elliptical, annular apertures such that the total H_{160} light of each galaxy is divided equally between three annuli. The galaxy core corresponds to the “inner” aperture, and the galaxy outskirts correspond to the “outer” aperture. The color gradient of the galaxy is denoted by

$$\Delta(m_1 - m_2) = (m_1 - m_2)_{\text{outer}} - (m_1 - m_2)_{\text{inner}}, \quad (1)$$

where m_1 and m_2 are the respective apparent magnitudes. A galaxy where the core has a redder color than the outskirts will have a negative color gradient, and a galaxy with a bluer core than the outskirts will have a positive gradient.

2.7. Star Formation Rates

In this work, we measure the total SFR as the sum of the SFR implied by the observed UV luminosity (uncorrected for dust extinction, SFR_{UV}) and by the IR (as estimated from the $24\ \mu\text{m}$ luminosity, SFR_{IR}). We convert the observed $24\ \mu\text{m}$ luminosity into an SFR using the empirical relationship from Wuyts et al. (2011a). For galaxies that are not detected in $24\ \mu\text{m}$, the SFRs are based on an attenuation-corrected UV flux using the attenuation value estimated by FAST, so $\text{SFR}_{\text{Total}} = \text{SFR}_{\text{UV}} \times \text{Correction}$. In both instances, we follow Kennicutt (1998) to convert the luminosity to SFR. The Kennicutt (1998) conversion is Salpeter-based, whereas the masses and other derived quantities are Chabrier-based. To account for the difference in IMF, we divide the total SFR by 1.66, $\text{SFR}_{\text{Total}} = (\text{SFR}_{\text{UV}} + \text{SFR}_{\text{IR}})/1.66$.

2.8. Discrete Star-forming Regions

In Section 5.6 we compare the ICD measurements to the frequency of discrete star-forming regions (colloquially “clumps”) in galaxies using the clump catalog of Guo et al. (2014). In order to facilitate clump finding, Guo et al. (2012) require galaxies to be approximately face-on ($b/a > 0.5$),

reasonably extended ($R_e > 0''.2$), and with a sufficient brightness ($H_{160} < 24.5$ mag).

Individual clumps are selected from the UV luminosity contrast between the individual clump and the total galaxy. From the catalog, we select clumps with UV luminosity $>1\%$ of the total galaxy UV light ($L_{\text{clump}}/L_{\text{galaxy}} > 0.01$) contained within galaxies in our sample. While Guo et al. (2014) select clumps with UV luminosity $>8\%$, we lower this threshold to include more UV-faint clumps as they are redder and provide a more comprehensive view of the ICD. This provides clump measurements for 180 objects, containing between zero and eight clumps per galaxy.

3. THE INTERNAL COLOR DISPERSION

3.1. Definition

First developed by Papovich et al. (2003), the ICD is a flux-independent statistic, defined as the ratio of the squared difference of the image flux-intensity values about the mean galaxy color to the square of the total image flux, or,

$$\xi(I_1, I_2) \equiv \frac{\sum_{i=1}^{N_{\text{pix}}}(I_{2,i} - \alpha I_{1,i} - \beta)^2 - \sum_{i=1}^{N_{\text{pix}}}(B_{2,i} - \alpha B_{1,i})^2}{\sum_{i=1}^{N_{\text{pix}}}(I_{2,i} - \beta)^2 - \sum_{i=1}^{N_{\text{pix}}}(B_{2,i} - \alpha B_{1,i})^2} \times 100\%. \quad (2)$$

The ICD assesses the morphological difference of a galaxy between two passbands. The rest-frame UV–optical ICD quantifies the spatial homogeneity (or lack thereof) between young stellar populations (dominating the rest-frame UV light) and older stellar populations, contributing most of the rest-frame optical light. Galaxies with spatially segregated stellar populations with different colors would have large ICD (see Papovich et al. 2003), whereas, a galaxy with a homogeneous stellar population throughout would have a low ICD.

The terms in Equation (2) sum over $i = 1 \dots N_{\text{pix}}$, with N_{pix} being the number of pixels associated with each galaxy; I_1 and I_2 are the image flux-intensity values for each object obtained in each of two passbands, and B_1 and B_2 are the pixel intensity values from a contiguous, similarly sized region of the two passbands not associated with any object.

To determine which pixels belong to a galaxy, we define the aperture size as r_p ($\eta = 0.2$), where r_p is the Petrosian radius of I_2 as defined for the Sloan Digital Sky Survey (Blanton et al. 2001), and $\eta(r)$ is defined as the ratio of the galaxy surface brightness, $I(r)$, averaged over an annulus of radius r , to the mean surface brightness within this radius, $\langle I(r) \rangle$. The Petrosian radius depends on the surface brightness distribution of the galaxy and is thus independent of redshift or systematics in the image calibration. The chosen aperture encompasses most of the light from the galaxy without adding excessive background light. Therefore, the summations are over the individual pixels associated with the object or blank region of a similar size.

The scaling factor α is the ratio of total fluxes between images I_2 and I_1 , while the linear offset β adjusts (if necessary) for differences in the relative background levels of the two images. In practice, we calculate these terms by minimizing the statistic, $\chi^2 = \sum [(I_2 - \alpha I_1 - \beta)/\sigma]^2$, adjusting α and β as free parameters (where σ represents the uncertainties on the I_2 flux intensity values).

The treatment of the background terms (B_1 and B_2) is important to the ICD, as the background itself can contain an intrinsic amount of ICD based on our definition. Therefore, to eliminate ICD contribution from the background, B_1 and B_2 are selected for each individual galaxy to contain the same number of pixels (N_{pix}) at random locations excluding any preexisting objects, and include the same pixels in both image 1 and 2. In order to minimize the ICD variations due to background, we select the median ICD value computed from using nine different background regions. However, simple fluctuations may not be the only source of ICD. Because the WFC3 imaging PSF has been convolved (see Section 2) to match that of the ACS, there exists the possibility of correlated noise in the background measurements. This could have an effect if the background region is not selected in the same way as the galaxy (e.g., choosing individual pixels at random versus a single contiguous region). We test for possible effects by choosing individual pixels not associated with an object at random from the imaging, choosing a single contiguous *square* region and contiguous *circular* region. We find no effect based on the morphology of chosen background pixels.

3.2. ICD Dependence on Signal-to-noise Ratio (S/N)

Previous studies (Papovich et al. 2003, 2005; Bond et al. 2011) noted that the ICD produces unreliable results for galaxies with low S/N. We test the behavior of the ICD using simulated galaxies with a priori known (fixed) total flux and ICD. Each simulated galaxy is placed throughout the *HST* images at a random location and is then checked to ensure no overlap with an actual object by comparing the location with the `SEXTRACTOR` segmentation image. The flux of the galaxy is slowly decreased to a level barely above the background. We then derive an ICD value for each simulated object using the definition in Equation (2).

Figure 1 shows the fractional change (true minus observed divided by true) in the ICD as a function of $S/N = \sum f / \sqrt{\sum \sigma^2}$, where f represents the flux intensity values and σ^2 is the image variance due to the noise of the background. The sum is taken over all pixels identified as belonging to the object, by computing the Petrosian radius and comparing the enclosed pixels to the `SEXTRACTOR` segmentation image. The four simulated objects illustrate how different levels of ICD (2%, 6%, 13%, and 26%) are effected by the galaxy’s S/N.

The behavior of the fractional change is dramatically different depending on whether a galaxy has intrinsically “low” or “high” ICD. For all galaxies with very high S/N we recover the expected ICD to within 0.1%. However, as the S/N decreases, Equation (2) systematically *underestimates* the ICD. This bias is most apparent for galaxies with “low” intrinsic ICD.

Because of the systematic underestimation of the ICD, it is important to clip the sample at an S/N that still provides accurate results. We choose $S/N = 10$ such that the bias does not impact our results. For objects with $S/N = 10$ and high intrinsic ICD ($\xi_{\text{true}} > 6\%$), the bias is small, with fractional changes ($\xi_{\text{true}} - \xi_{\text{observed}}/\xi_{\text{true}}$) of $<34\%$, and the bias decreases for objects with increasing ICD. The bias increases for objects with lower intrinsic ICD, such that the fractional change is 100% for objects with $S/N = 10$ and $\xi_{\text{true}} = 2\%$. This is acceptable because the ICD increases by only a factor of 2. Therefore, to our $S/N = 10$ limit, we can be confident that

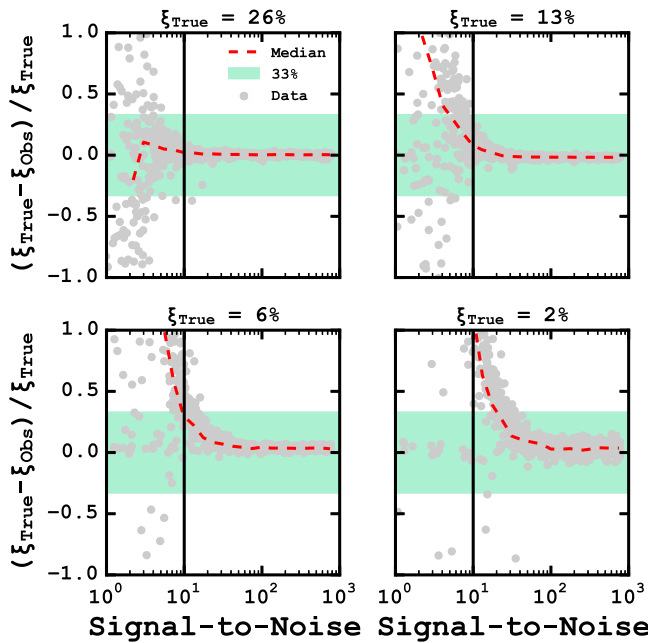


Figure 1. Fractional change of the ICD as a function of S/N for two different simulated objects. Gray points show individual S/N measurements. Red dashed lines show the median value. Green shaded regions show the area where the fractional change is less than 33% from the true value and serves as an aid to gauge accuracy. For the low ICD galaxy (top panel) we find that for galaxies with $S/N < 10$ in the *bluer band* the median ICD deviates more than 34% away from the true value. Therefore, we remove any objects from our initial sample that have $S/N \geq 10$ in the bluer band. The S/N requirement for galaxies with intrinsically high ICD could be set to a lower threshold, but we choose a constant criterion to keep the selection uniform.

objects with observed high ICD have high intrinsic ICD, and objects with low observed ICD have low intrinsic ICD.

In principle, this S/N requirement applies to both bands used in Equation (2). However, for this particular study, the redder band (namely, H_{160}) S/N is much higher in the majority of galaxies analyzed, such that this requirement, in practice, only applies to the bluer imaging band. It is also important to note that this S/N does not correspond to a single bluer band magnitude limit, because at fixed magnitude a larger object (with lower surface brightness) will have a lower S/N . For galaxies with an intrinsic ICD very near zero and low surface brightness in the bluer band, it is possible for the ICD calculation to produce negative results when the background contributes significantly to the fluctuations. Galaxies with an intrinsically larger ICD are more resistant to surface brightness dimming as the fluctuations of the galaxy dominate those of the background.

After applying the $S/N = 10$ restriction in i_{775} , we have a final, primary sample of 2601 galaxies. Unfortunately, this S/N requirement leads to a selection effect where we prefer galaxies with some level of active star formation, as passively evolving galaxies often do not have enough blue light to be included in this analysis. The effect of this selection bias is discussed further in Section 4.1.

3.3. Error Associated with ICD

Papovich et al. (2003) define the statistical error associated with the ICD, assuming that the background pixels (those not

associated with any galaxy) are normally distributed, as

$$\delta(\xi) = \frac{\sqrt{2/N_{\text{pix}}} \sum_{i=1}^{N_{\text{pix}}} (B_{2,i}^2 + \alpha^2 B_{1,i}^2)}{\sum_{i=1}^{N_{\text{pix}}} (I_{2,i} - \beta)^2 - \sum_{i=1}^{N_{\text{pix}}} (B_{2,i} - \alpha B_{1,i})^2}. \quad (3)$$

Papovich et al. (2005) note that Equation (3) underestimates the uncertainties associated with the ICD. They estimated that the uncertainties for Equation (2) in their data required corrections of factors of 6–7 to account for correlated noise in the images. Bond et al. (2011) find that even after the correction suggested by Papovich et al. (2005), the uncertainties on the ICD obtained for bright objects (those with low errors) are underestimated by as much as a factor of three, the dominant source of error being contributions from non-uniform sky backgrounds and PSF mismatch between the two passbands.

For this work, we use the observed ICD values for different levels of intrinsic ICD and galaxy S/N to estimate the error associated with each measurement. To estimate the systematic uncertainty, we compare the median ICD fractional change (the dashed line in Figure 1) to the true value, and to estimate the statistical uncertainty, we compute the median absolute deviation.

In all cases, galaxies with very high ($S/N_{i_{775}} > 100$) S/N have low ($< 1\%$) systematic uncertainties and very low ($\ll 0.2\%$) statistical uncertainties. The closer to our $S/N_{i_{775}}$ cutoff ($S/N_{i_{775}} = 10$), the systematic error, described in the previous section, increasingly dominates. The statistical uncertainty remains very low, $\sim 0.2\%$, and so we neglect any effect due to the statistical variation in the ICD.

4. THE RELATION BETWEEN GALAXY PROPERTIES AND ICD

For the majority of our results we choose to use $\xi(i_{775}, H_{160})$ as our primary diagnostic. For the galaxies in our sample, these two filters span the Balmer/4000 Å break over $z \sim 1.5-3$ and allow us to compare the rest-frame UV (traced by the i_{775} band) to the rest-frame optical (traced by the H_{160} band). This provides us the ability to investigate recent star formation (with i_{775}) and past-averaged star formation (with H_{160}). In Section 5.4 we make use of a different version of the ICD, namely, $\xi(V_{606}, J_{125})$, which allows us to compare slightly different parts of each galaxy’s spectral energy distribution to better understand the results given by $\xi(i_{775}, H_{160})$.

The median ICD for the full sample is $\xi(i_{775}, H_{160}) \simeq 5\%$. In the sections that follow we refer to galaxies with ICD value above and below this median as high and low ICD, respectively.

4.1. The ICD versus Galaxy Mass

Stellar mass is one of the most fundamental properties of galaxies. The stellar mass of a galaxy correlates with many of its physical properties, including overall color (Grützbauch et al. 2011) and SFR (e.g., Daddi et al. 2007; Magdis et al. 2010), to $z \sim 3$ (and perhaps beyond; e.g., Salmon et al. 2014). As such, it is possible to gain much insight into the formation and evolution of galaxies through the rates of change of the ICD as functions of stellar mass.

Figure 2 shows the $\xi(i_{775}, H_{160})$ as a function of stellar mass for the galaxies in our sample. We find that the median

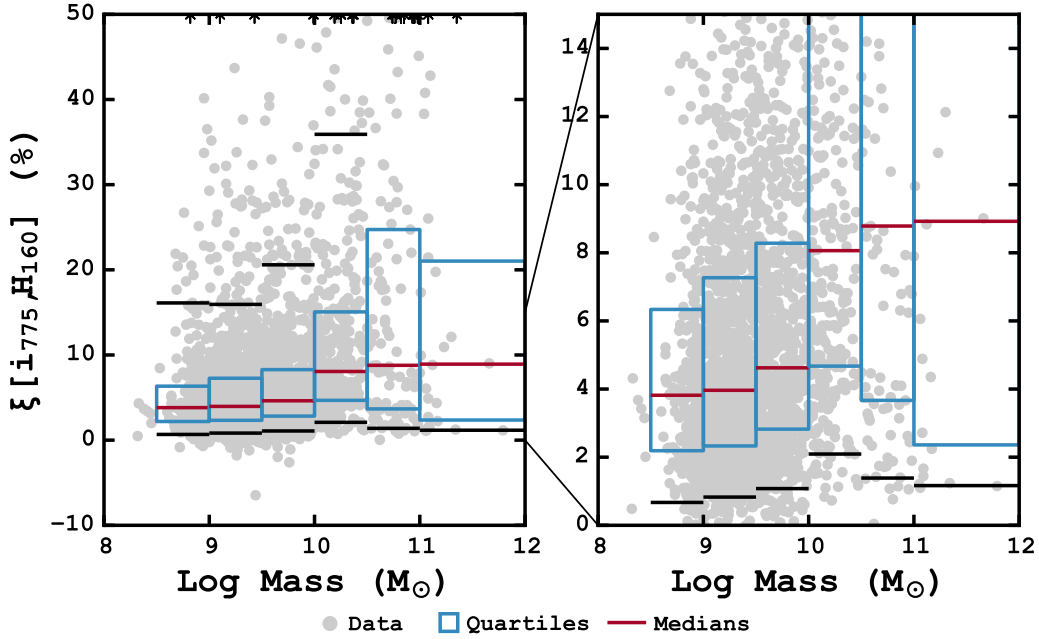


Figure 2. ICD as a function of galaxy stellar mass. Individual galaxies are shown as gray points. The galaxies are then binned together by stellar mass in bins of 0.5 dex (except for the highest mass bin, which is 1.0 dex) beginning with $\log (M/M_{\odot}) = 8.5$. The upper and lower quartiles of ICD are indicated by the blue boxes. The median of each bin is indicated by the red line. The upper and lower black bars show the 95th and 5th percentiles, respectively. The ICD for galaxies in our sample is low for low stellar masses, peaks in the intermediate stellar masses, and returns to low values at high stellar masses.

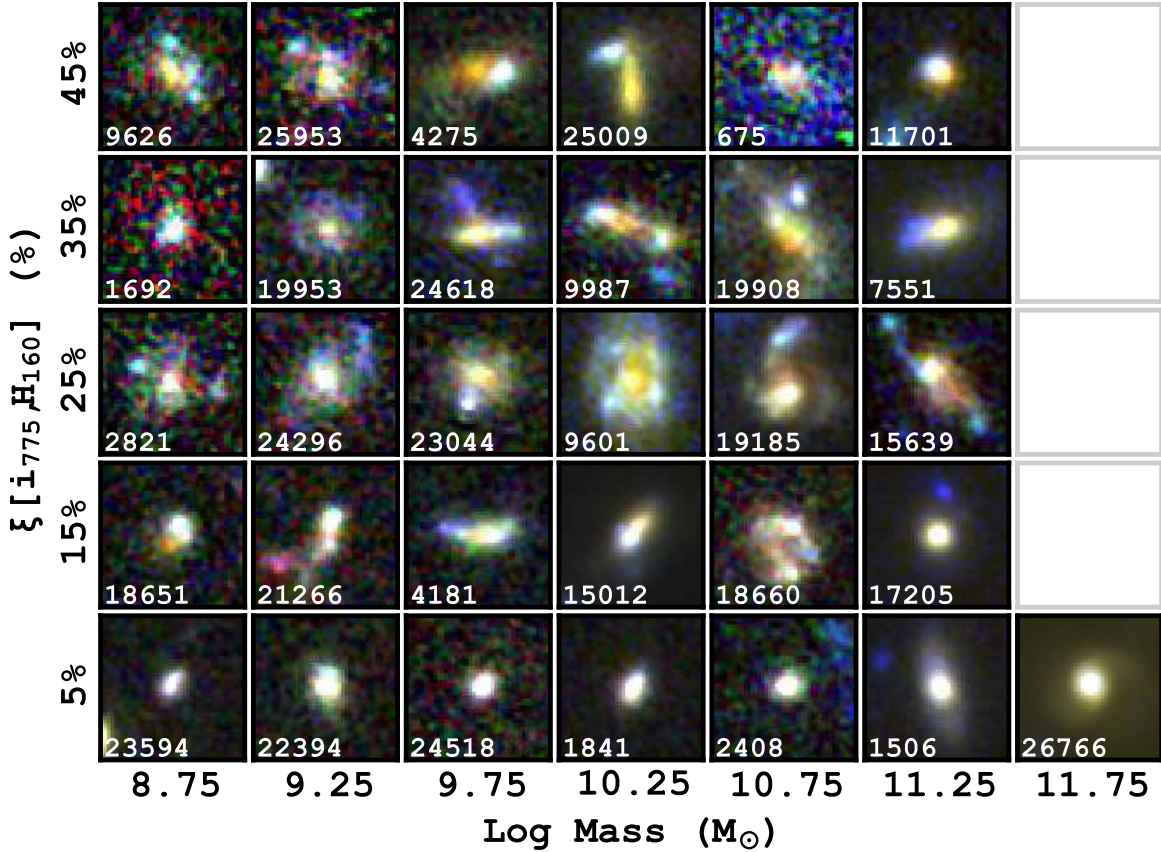


Figure 3. Galaxy montage showing examples of galaxies as a function of their location on the ICD—stellar-mass plane. Columns are bins of stellar mass, while rows are bins of ICD. The RGB images are combinations of H_{160} , J_{125} , and i_{775} . Galaxies with elevated ICD values ($\xi(i_{775}, H_{160}) > 15\%$) and stellar masses $\log (M/M_{\odot}) = 10$ –11 appear significantly different than the galaxies in either other stellar mass bins or galaxies with depressed ICD values. Each cutout is $2''$ on the sky regardless of the redshift of the object, which corresponds to ~ 20 kpc over the redshift range. Galaxies filling the grid are selected at random from all galaxies falling into the bin. Empty squares indicate regions in the $\xi(i_{775}, H_{160})$ -mass space where there are no galaxies in our sample. The labels represent the centers of either the ICD or stellar mass bins. So a galaxy in the bottom left corner (e.g., 23594) could have a stellar mass $8.5 < \log (M/M_{\odot}) < 9$ and an ICD of $0\% < \xi(i_{775}, H_{160}) < 10\%$.

$\xi(i_{775}, H_{160})$ values in the three low stellar mass bins are between 3.5% and 4.5%, the median ICD value in the moderate stellar mass bin is above 8%, and at stellar masses $\log(M/M_{\odot}) > 11$, we find that galaxies have a median ICD value about 9%. If we take into account the systematic underestimations of low ICD values, discussed in Section 3.3, we find little relative change in the median $\xi(i_{775}, H_{160})$ between bins, in that the moderate stellar mass bins still show higher $\xi(i_{775}, H_{160})$ medians than the bins of lower stellar masses.

To illustrate the ICD, Figure 3 shows galaxy images in the $\xi(i_{775}, H_{160})$ -mass plane. The galaxies are selected at random from all of the galaxies contained in each bin of mass and $\xi(i_{775}, H_{160})$. The RGB images are combinations of H_{160} , J_{125} , and i_{775} . Galaxies with elevated ICD values (top rows) and in the moderate stellar mass range appear significantly different from the galaxies in other stellar mass bin or galaxies with lower ICD values. Visually, galaxies with high ICD have morphologies with well-separated regions of rest-frame UV (blue) and rest-frame optical (red) light. Galaxies with low ICD values tend to have smooth morphologies and uniform colors, suggesting fewer regions of separated red and blue emission.

4.1.1. High-mass Galaxies

The highest stellar mass galaxies ($\log(M/M_{\odot}) > 11$) deserve special attention. Because the S/N threshold applies only to the bluer band used in the ICD calculation, galaxies that are well detected in H_{160} may not be well detected in i_{775} . Specifically, massive galaxies often have the reddest i_{775} - H_{160} colors, so we expect that many of them have high H_{160} S/N and low $S/N_{i_{775}}$. The concern is that these objects could have higher intrinsic ICD but are excluded because of our S/N requirement (see Section 3.2).

To investigate this possibility, we compare the mean $i_{775} - H_{160}$ color of the high stellar mass galaxies included and excluded from our sample. Galaxies that have $S/N_{i_{775}} \geq 10$ have $\langle i_{775} - H_{160} \rangle = 2.6$ mag, while galaxies with $S/N_{i_{775}} < 10$ have $\langle i_{775} - H_{160} \rangle = 3.4$ mag. This suggests that the excluded high stellar mass galaxies simply do not have enough blue light to produce high ICD values. Papovich et al. (2005) simulate just such a situation, where the authors find that extremely red galaxies, even with the addition of highly star-forming regions, produce nearly no ICD as the older stellar populations simply overwhelm any diversity. For the seven high stellar mass galaxies with $i_{775} - H_{160} > 3$ mag in our sample, four have high $\xi(i_{775}, H_{160})$; however, after visual inspection the accuracy of the measured ICD becomes questionable (for reasons discussed below).

A visual inspection of the 26 most massive galaxies, shown in Figure 4, shows that the majority of these objects have smooth light profiles in both i_{775} and H_{160} . There are several exceptions that fall into two broad categories: galaxies that appear to have faint, nearby objects detected in i_{775} but not H_{160} (e.g., 16375, 17205, and 16934). Because H_{160} serves as the object detection image, it is possible that these faint objects lie within the H_{160} Petrosian radius used for the ICD calculation, contributing significantly to the measured ICD. While the origin of these nearby objects is unclear, possible scenarios include a chance alignment or a disrupted satellite. There are also galaxies in the highest stellar mass subsample with extended structures, showing distinct red/blue regions and

likely individual clumps of star formation embedded within the galactic structures (e.g., 282, 15639, and 15261). In both cases, these features contrast with the H_{160} -dominated central region producing the large $\xi(i_{775}, H_{160})$ value. The blue central regions in the $i_{775} - H_{160}$ color maps reflect small mismatches in the PSF matching (see van der Wel et al. 2012 for a description) and do not contribute significantly to the ICD as they are small compared to the total flux of the galaxy.

After a visual inspection, if we remove the galaxies with neighboring objects from the high stellar mass bin, the median $\xi(i_{775}, H_{160})$ becomes $\sim 7\%$. However, if we instead place a more stringent i_{775} S/N requirement (i_{775} S/N > 30) on the high stellar mass galaxies, we find that the median $\xi(i_{775}, H_{160})$ further drops to 3.3%.

Because it is unclear whether or not the faint objects neighboring the primary galaxy are physically associated with the primary, or are chance alignments along the line of sight, we do not exclude these objects and do not adjust the i_{775} S/N requirement. Instead, we note that these objects are infrequent in the sample and so do not affect our conclusions. So while the median $\xi(i_{775}, H_{160})$ in the high stellar mass bin may appear to be very similar to the moderate stellar mass bins, it is likely that the median is being inflated due to inclusion of galaxies with neighboring objects or galaxies with low i_{775} S/N and high H_{160} S/N.

4.2. The ICD versus Sérsic Profile

Many previous works (e.g., Blanton et al. 2003; Bell et al. 2012; van der Wel et al. 2012) use the Sérsic index to classify a galaxy's morphology. The Sérsic index parameterizes a galaxy's surface brightness profile, where $n = 4$ corresponds to a classical bulge, $r^{1/4}$ -law profile (de Vaucouleurs 1948) and $n = 1$ corresponds to the exponential profile of a galactic disk. We refer to galaxies with $n < 2$ as disk dominated and those with $n > 2$ as bulge dominated.

Figure 5 shows $\xi(i_{775}, H_{160})$ as a function of stellar mass, separated based on their Sérsic indices. Again, we divide the sample into mass bins, where each bin is 0.5 dex wide or larger to ensure there are at least 10 objects in each bin. Galaxies with high ICD prefer a lower Sérsic index (disk dominated). Inside the individual Sérsic bins, galaxies with intermediate stellar mass ($10 < \log(M/M_{\odot}) < 11$) display the largest ICD, but as the Sérsic index increases, the upper envelope of ICD values decreases: bulge-dominated ($n > 2$) galaxies have low ICD. For disk-dominated galaxies ($n < 2$) the median galaxy across all masses has a high ICD value.

The systematic underestimation described in Section 3.3 has very little effect on the preference of galaxies with low Sérsic index and intermediate stellar mass to have high $\xi(i_{775}, H_{160})$. This is because there is very little relative change in the medians of the bins due to the underestimation of the ICD.

There is a well-known trend between the Sérsic index and stellar mass, with the Sérsic index increasing with increasing stellar mass. This relationship is apparent at both low (e.g., Dutton 2009) and high (e.g., Franx et al. 2008; Bell et al. 2012) redshift. We find a similar trend. The three low Sérsic bins lack (or have very few) galaxies with masses greater than $\log(M/M_{\odot}) \sim 11$. In fact, it is only the highest Sérsic bin that shows any significant number of high stellar mass galaxies.

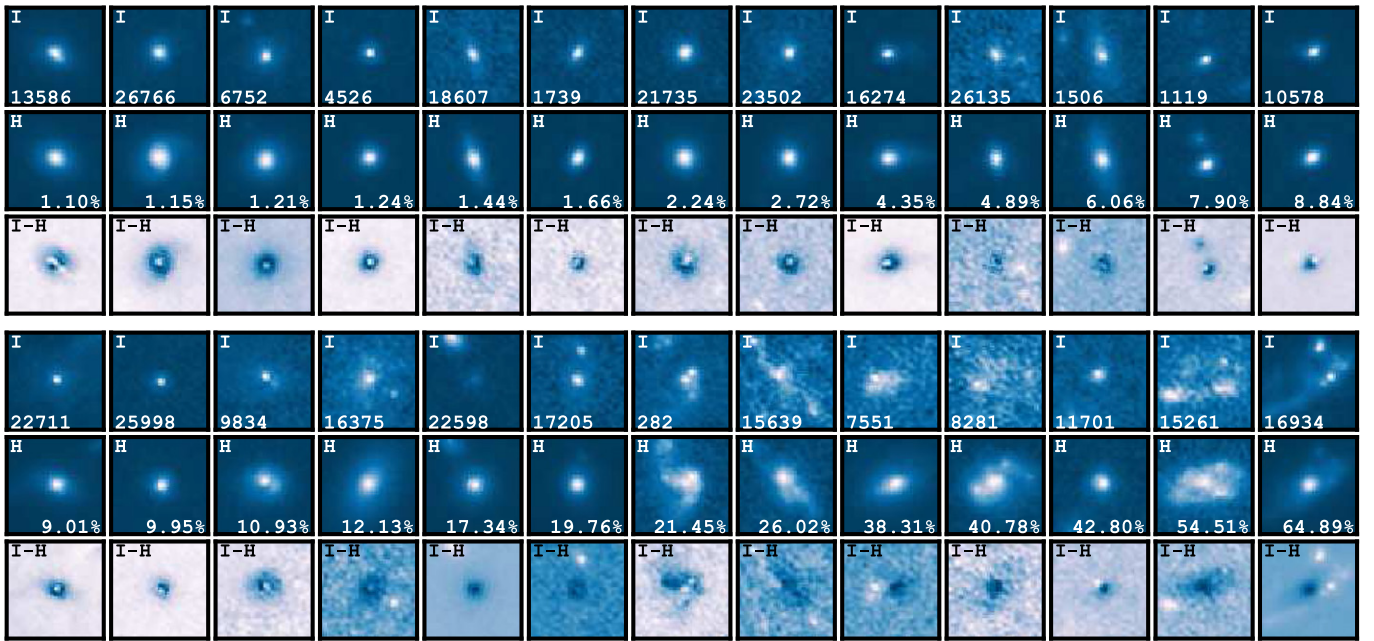


Figure 4. Galaxy montage of the high mass ($11 > \log(M/M_\odot)$) galaxies. Each triplet of panels shows either the i_{775} , H_{160} imaging or the $i_{775} - H_{160}$ color map, along with the ID number and associated $\xi(i_{775}, H_{160})$ value. Each cutout is $2''.5$ on the sky regardless of the redshift of the object, which corresponds to ~ 20 kpc over the redshift range. The panels are ordered from lowest to highest $\xi(i_{775}, H_{160})$.

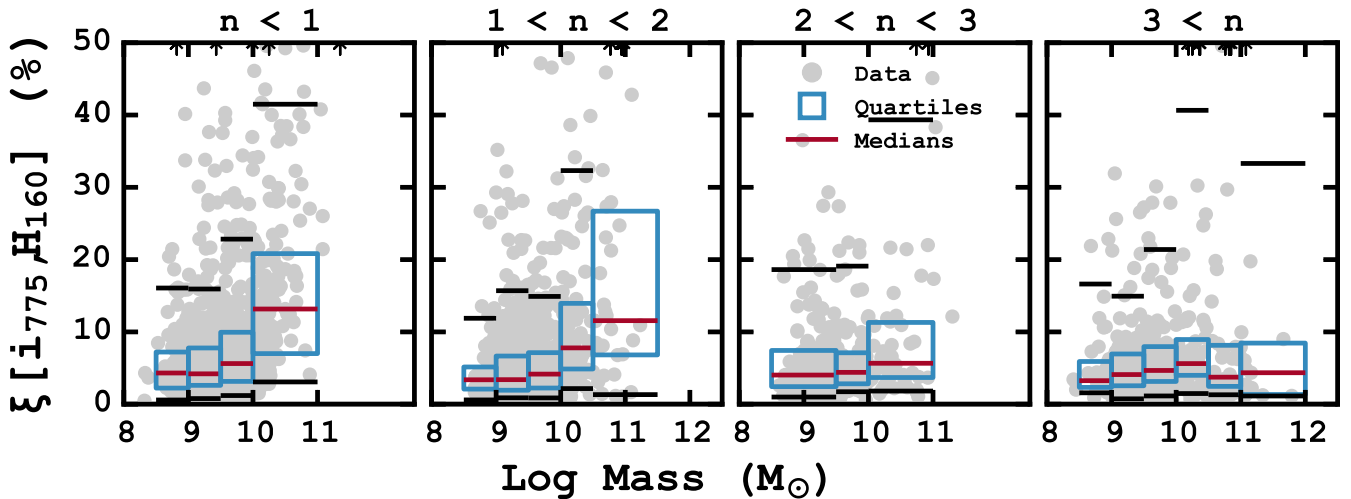


Figure 5. Galaxies binned into four bins of Sérsic index. The galaxies are then binned by stellar mass in bins of 0.5 dex beginning with $\log(M/M_\odot) = 8.5$. The upper and lower quartiles are indicated by the blue boxes. The median of each bin is indicated by the red line. The upper and lower bars show the 95th and 5th percentiles, respectively. We find that galaxies with high ICD (greater than 5%) are dominated by low Sérsic indices in general, suggesting that they either are disk galaxies or have high extinction.

4.3. The ICD versus Star Formation Rate

The ICD is sensitive to heterogeneities in the stellar populations of galaxies. One possible cause of these heterogeneities is unobscured, young stellar populations separated from older, passively evolving populations. Because young populations are needed to produce measurable ICD, the SFR of a galaxy could be closely related to the ICD. Figure 6 shows the sSFR, the SFR normalized by the galaxy’s stellar mass, as a function of $\xi(i_{775}, H_{160})$.

We find that the $\xi(i_{775}, H_{160})$ of a galaxy is not directly tied to its sSFR. Galaxies with low $\xi(i_{775}, H_{160})$ values show no correlation with sSFR; however, galaxies with high $\xi(i_{775}, H_{160})$ values show predominately “normal” sSFRs. For galaxies with low sSFRs we expect low $\xi(i_{775}, H_{160})$ values as such

galaxies have few young stellar populations producing the blue light needed to contrast the redder light from more evolved stellar populations. Galaxies showing very high sSFRs, often due to re-radiation by dust in the IR, also have low $\xi(i_{775}, H_{160})$, suggesting that dust variations play a small role in the production of ICD.

Again, this result is robust even after accounting for the systematic underestimate of the low $\xi(i_{775}, H_{160})$ galaxies. Shifting the lowest $\xi(i_{775}, H_{160})$ galaxies upward to higher $\xi(i_{775}, H_{160})$ values does not produce a trend with sSFR.

5. POTENTIAL DRIVERS OF THE ICD

As discussed previously, the ICD is sensitive to heterogeneous stellar population variations that give rise to

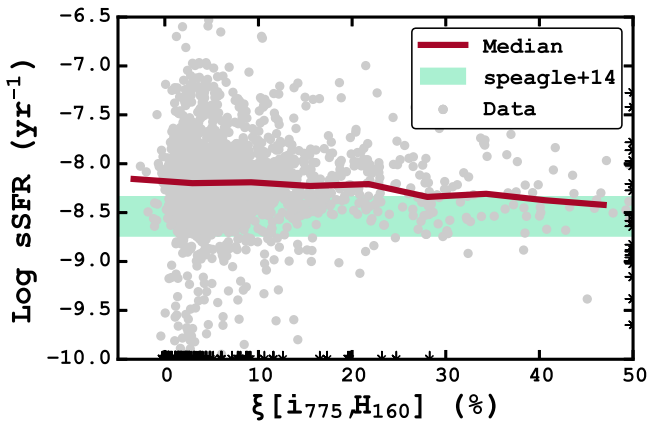


Figure 6. Galaxies’ sSFR as a function of $\xi(i_{775}, H_{160})$. The gray points are the actual data values, and the red line is the running median value. Galaxies that have been clipped for clarity are shown as black arrows. The shaded region shows the width of the star-forming “main sequence” for a $10^{10} M_{\odot}$ stellar mass galaxy at $z = 2.25$ taken from Speagle et al. (2014). We find that galaxies with the highest $\xi(i_{775}, H_{160})$ have very close to the median sSFR, while galaxies with the highest and lowest sSFRs lack many galaxies with very high $\xi(i_{775}, H_{160})$ values.

differences in the UV–optical flux ratio within a galaxy. In this section we discuss possible scenarios that could lead to high ICD. Specifically, we investigate whether merger activity, the galaxy’s physical size, intrinsic color gradients, effects due to redshift, or heterogeneous extinction drive increased ICD.

5.1. Mergers

Based on morphological asymmetries, Papovich et al. (2005) suggested that some of the galaxies with high ICD are likely the result of merger activity. To investigate this, we use non-parametric morphological indicators, specifically the Gini coefficient, G , and the second-order moment of the brightest 20% of a galaxy’s flux, M_{20} , to better understand the role of galaxy mergers in producing high ICD. Many studies demonstrate these parameter’s usefulness in quantifying galaxy morphology in large samples at both low and high redshifts (e.g., Lotz et al. 2004; Abraham et al. 2007; Law et al. 2007, 2012; Wang et al. 2012; Lee et al. 2013).

Lotz et al. (2008) adopt the following classification scheme based on G – M_{20} :

$$\begin{aligned}
 \text{Mergers} : G &> -0.14 M_{20} + 0.33 \\
 \text{E/S0/Sa} : G &\leq -0.14 M_{20} + 0.33 \text{ and} \\
 &G > 0.14 M_{20} + 0.80 \\
 \text{Sb - Ir} : G &\leq -0.14 M_{20} + 0.33 \text{ and} \\
 &G \leq 0.14 M_{20} + 0.80.
 \end{aligned} \tag{4}$$

Figure 7 shows the G and M_{20} values for the galaxies in our sample broken into large bins of ICD. As can be seen, mergers are not a dominant driver of the ICD. The majority of galaxies with high ICD values (5%–20%) prefer disk-dominated morphologies, consistent with our findings between the ICD and Séric index above. This suggests that mergers are not a significant cause of elevated ICD, except, possibly, at the highest levels ($\xi(i_{775}, H_{160}) > 20\%$), where 21% of galaxies are classified as mergers.

Given the small number of galaxies in the highest $\xi(i_{775}, H_{160})$ bin, we use a series of Monte Carlo simulations to estimate how often we would find a similar distribution simply

by chance. We assign each galaxy a morphology based on their location in the G – M_{20} space while allowing their $\xi(i_{775}, H_{160})$ to be changed. We then select galaxies with $\xi(i_{775}, H_{160}) > 20\%$ and record the fraction classified as mergers. We find that galaxies in the highest ICD bin are at least 21% mergers only 1.32% of the time. Or, given just random chance, 98.7% of the time we find fewer mergers in the highest ICD bin than what is actually measured.

5.2. Physical Size

The ICD requires that we are able to resolve scales to a minimum of 0.5 kpc (Papovich et al. 2003). Below this, the resolution of the image suppresses any ICD that may be present. Here we also considered how the ICD values change with increasing physical size.

Figure 8 shows $\xi(i_{775}, H_{160})$ as a function of semimajor axis, R_e . For galaxies with R_e below 3 kpc the median ICD remains low ($\sim 5\%$). Considering only the intermediate stellar mass ($10 < \log(M/M_{\odot}) < 11$), we find that ICD values remain low until ~ 2.5 kpc, after which it increases. In either case, we find more galaxies with large ICD at large R_e . However, this is most likely a selection effect where we are more able to detect ICD in extended objects. Furthermore, placing the galaxies on a size–mass relation provides a similar result. At a fixed stellar mass, we find more elevated $\xi(i_{775}, H_{160})$ galaxies with larger radii than at small radii.

One of our findings is that the ICD values are low for lower stellar mass galaxies, $\log(M/M_{\odot}) < 10$. Because these galaxies have lower R_e compared to higher stellar mass galaxies (e.g., Franx et al. 2008; Williams et al. 2010), we test if the trend between ICD and R_e affects this finding. We remove all objects with $R_e < 2$ kpc (at all stellar masses) and recompute how the median ICD changes as a function of stellar mass. The median $\xi(i_{775}, H_{160})$ for $\log(M/M_{\odot}) < 10$ remains low, with $\xi(i_{775}, H_{160})_{\text{median}} \simeq 5\%$. The median $\xi(i_{775}, H_{160})$ for moderate stellar mass galaxies remains elevated, $\xi(i_{775}, H_{160})_{\text{median}} > 10\%$, for $10 < \log(M/M_{\odot}) < 11$, and the $\xi(i_{775}, H_{160})$ declines at the highest stellar masses. Therefore, the relation between ICD and R_e does not dominate our conclusions between ICD and stellar mass.

5.3. Color Gradients

Galaxies show a radial color gradient when the color of the light in an annulus on the outskirts differs from the color inside a central region (see Section 2.6). For galaxies with large color gradients, this difference could potentially lead to large ICD values. Szomoru et al. (2011) found that the majority of a mass-selected sample from the HUDF shows negative color gradients (redder cores and bluer outer regions). We find a similar result for the galaxies in our sample, with an average color gradient $\Delta(i_{775} - H_{160}) = -0.12$ and 66% of the sample showing a negative color gradient.

The relationship between color gradient and the ICD is complex. Figure 9 shows $\Delta(i_{775} - H_{160})$ as a function of $\xi(i_{775}, H_{160})$. We find that while galaxies with high ICD typically have negative color gradients, there is no correlation between the strength of the color gradient and the ICD. Therefore, while strong color gradients do not necessarily imply high ICD values, galaxies with high ICD appear to require larger color gradients, either positive or negative.

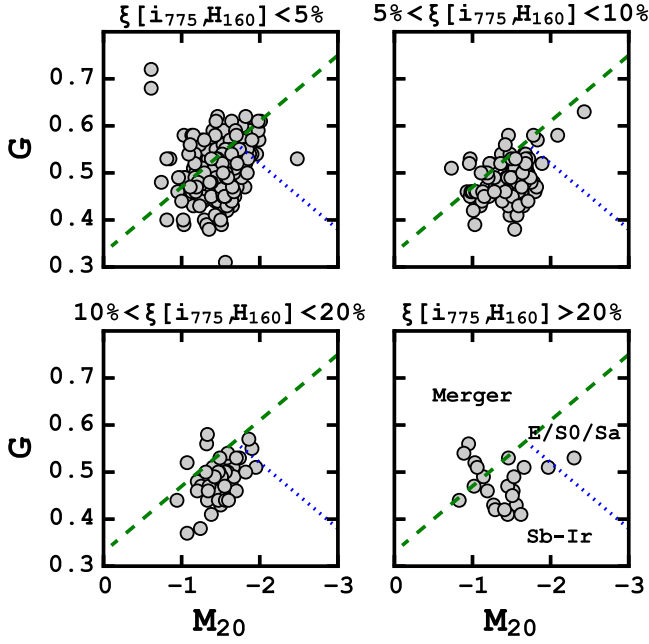


Figure 7. Morphological classification ($G-M_{20}$) of objects in our sample. Based on this classification scheme, objects above the dashed green line are mergers, below the dashed green line but above the blue dotted line are elliptical galaxies, and below both lines are spiral galaxies. The majority of galaxies with $\xi(i_{775}, H_{160}) > 5\%$ are not classified as mergers.

To understand how much a color gradient contributes to the measured ICD, we perform the following test. We mask the central $0''.18$ (~ 1.5 kpc) of all galaxies and recompute the ICD value. Figure 10 shows the relative change in the ICD due to this masking. In the majority of galaxies with small $\xi(i_{775}, H_{160})$ values, removing the nuclear region causes the ICD to decrease, while in galaxies with larger ICD values there is little change. This is as expected for galaxies with small ICD values as masking out the central regions also removes some of the variation. Therefore, while galaxies with strong color gradients may have high ICD, this is not a requirement. The observed color gradients alone are insufficient to produce the ICD in the galaxies in our sample.

5.4. Redshift Effects from Bandpass Shifting on the ICD

The galaxies in our sample span a range of redshift from $1.5 < z < 3.5$. As a result, the rest-frame light probed by both i_{775} and H_{160} varies between galaxies. For example, in galaxies at $z = 1.5-2.5$, H_{160} probes rest-frame $4600-6400 \text{ \AA}$, while at higher redshifts, $z > 3$, H_{160} probes light shortward of 4000 \AA . Therefore, we have considered how the variation in rest-frame light could affect our ICD measurement.

For galaxies at $z < 2$, we measure the ICD between V_{606} and J_{125} , as these bandpasses observe similar rest-frame wavelengths as i_{775} and H_{160} for galaxies at $z > 2.2$. Figure 11 shows ICD as a function of redshift where we have binned the galaxies by redshift. The top row of Figure 11 shows $\xi(i_{775}, H_{160})$, and the bottom shows $\xi(V_{606}, J_{125})$. For the comparable bins ($z = 1.5-2$ for $\xi(V_{606}, J_{125})$ and $z \sim 2.2$ for $\xi(i_{775}, H_{160})$) we find very little ($< 0.1\%$) difference between the median ICD values. This shows that as long as the imaging bands chosen to calculate the ICD span the rest-frame Balmer/4000 \AA break, we calculate a similar ICD.

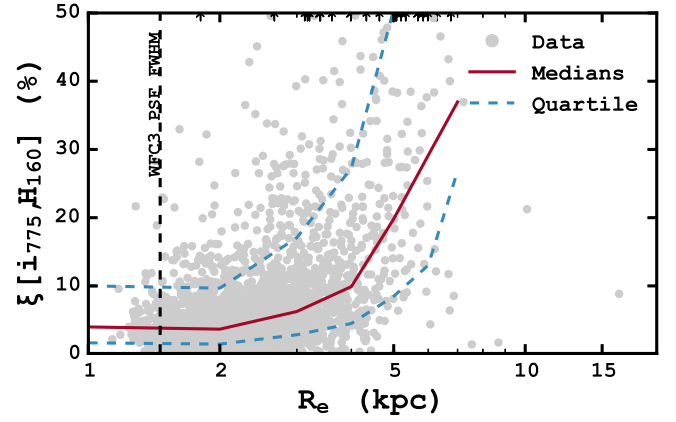


Figure 8. $\xi(i_{775}, H_{160})$ as a function of the galaxy's effective radii (semimajor axis). Gray points are the individual galaxies. The red line is the median $\xi(i_{775}, H_{160})$ value, and the blue dashed line represents the interquartile range, 75%, and 25%, respectively. The dashed vertical line shows the effective radius corresponding to the FWHM of the WFC3 PSF ($\text{FWHM} = 0''.2$) at $z = 3.5$. We find no trend suggesting a preference of physical size for a galaxy with elevated ($\sim 7\%$) $\xi(i_{775}, H_{160})$.

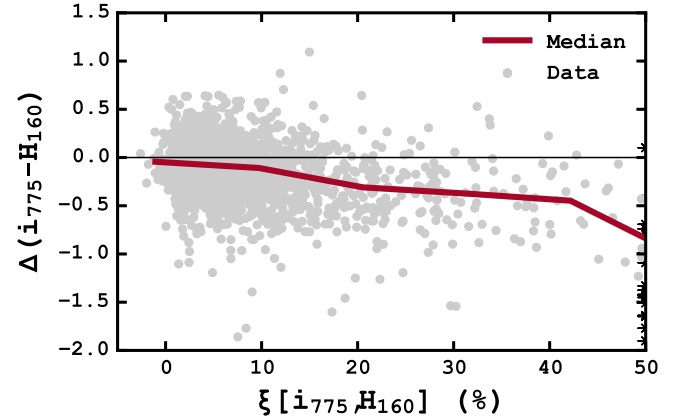


Figure 9. Galaxy's color gradient, $\Delta(i_{775} - H_{160})$, as a function of $\xi(i_{775}, H_{160})$. Gray points are the data, and the red line is the median color gradient as a function of ICD. We find that galaxies with high ICD have systematically lower color gradients, suggesting that they have redder cores than outskirts.

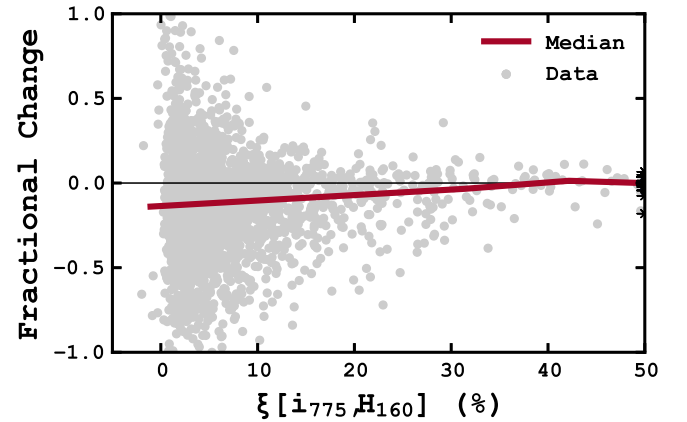


Figure 10. Fractional change between the $\xi(i_{775}, H_{160})$ calculated with the center $0''.18$ removed and the $\xi(i_{775}, H_{160})$ calculated for the entire galaxy as a function of $\xi(i_{775}, H_{160})$ for the entire galaxy. We find that galaxies with their centers removed show an elevated amount of $\xi(i_{775}, H_{160})$. This is expected as the variations in the outskirts play a more significant role with the bright central region removed, indicating that the observed ICD is not due to an underlying color gradient.

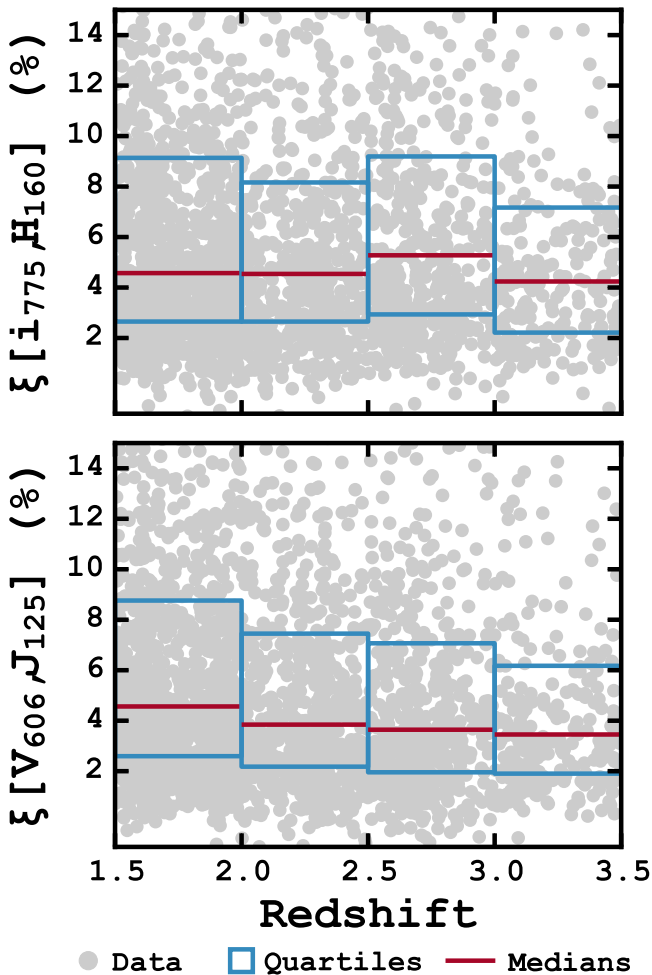


Figure 11. ICD of galaxies in our sample as a function of redshift. The galaxies are then binned together by redshift in bins of 0.5 dex beginning with $z = 1.5$. The upper and lower quartiles are indicated by the blue boxes. The median of each bin is indicated by the red line. For clarity, only a portion of the possible ICD range is shown. Top and bottom panels show $\xi(i_{775}, H_{160})$ and $\xi(V_{606}, J_{125})$ as a function of redshift, respectively. In both panels we do not see a significant increase in the median values of ICD. The inclusion of the bluer bands (V_{606} and J_{125}) acts as a probe for bandpass shifting effects. Because neither shows a significant trend, this suggests that the lack of increased values is not simply due to bandpass shifting effects.

For galaxies above $z = 3$ both i_{775} and H_{160} lie blueward of the rest-frame Balmer/4000 Å break, and Bond et al. (2011) suggest that a sharp downturn would be observed as the ICD probes similar populations. We find no such downturn, suggesting that while the Balmer/4000 Å break is moving through H_{160} , the observed trends in $\xi(i_{775}, H_{160})$ as a function of stellar mass (Figure 2) are not simply due to the effect of redshift, but due to the individual characteristics of the galaxies.

5.5. Effects of Dust Attenuation on the ICD

As mentioned earlier, high ICD could result from spatial variations of stellar ages or dust attenuation. In this section, we investigate whether the ICD is related to the total dust content of our galaxies.

If inhomogeneous attenuation (the reddening of selective parts of a uniformly blue population) is the primary driver of the ICD, then we would expect to find galaxies with both very

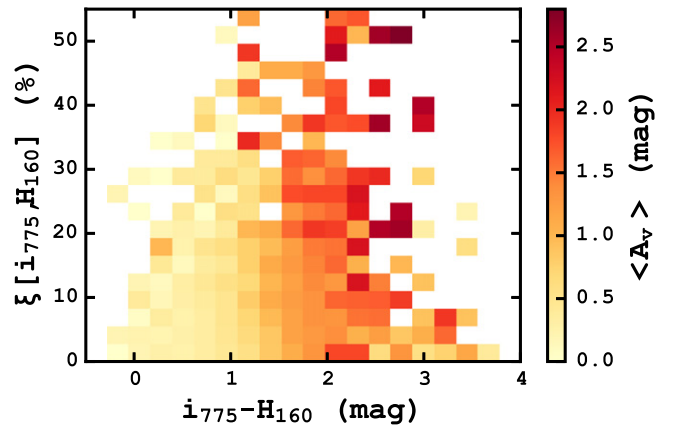


Figure 12. ICD as a function of $i_{775} - H_{160}$ color. The colored boxes show the average attenuation value (A_V) of the points within the region. For the galaxies in our sample, we find no evidence of a correlation between the measured stellar population diversity and the rest-frame UV–optical color. We do find that galaxies with large ICD values also show large attenuation values.

red colors and high ICD values. A uniformly blue galaxy would begin with a blue $i_{775} - H_{160}$ color, and if we were to add a level of inhomogeneous dust, then we would expect the ICD to rise, as there is now red light with which to contrast the blue and the overall color to shift toward the red. Similarly, if a galaxy with a heterogeneous stellar population has the young star-forming regions attenuated, then the ICD would go down as there is less blue light contrasting the red and the $i_{775} - H_{160}$ color again shifts toward the red. Finally, if a galaxy dominated by older stellar populations is dust attenuated, then the red stellar populations become redder, shifting the $i_{775} - H_{160}$ color, but the ICD would increase as there is now some contrast between stellar populations.

In Figure 12 we show the ICD as a function of $i_{775} - H_{160}$ color and attenuation value (A_V) as reported by FAST (see Section 2.4). There is little evidence for a correlation between the ICD and A_V as we find high $\xi(i_{775}, H_{160})$ galaxies for a wide range of colors and A_V . The ICD is low for galaxies with both high and low $i_{775} - H_{160}$ colors, but galaxies with moderate $i_{775} - H_{160}$ color ($1 \text{ mag} < i_{775} - H_{160} < 2 \text{ mag}$) show the largest range in the ICD. Therefore, it seems that galaxies with moderate $i_{775} - H_{160}$ colors are required for high ICD, but color alone is not enough to predict high ICD. Papovich et al. (2005) and Bond et al. (2011) argue that this lack of direct correlation supports the idea that the ICD depends on spatial variations in the ages of the stellar populations and not dust attenuation.

As a second investigation, we compare the ratio of the total galaxy SFR ($\text{SFR}_{\text{total}}$), derived from the IR and UV emission (see Section 2.7), against the SFR inferred from the UV measurement (uncorrected for dust attenuation). In this way, the ratio of $\text{SFR}_{\text{total}}/\text{SFR}_{\text{UV}}$ is a measure of the amount of light from star formation that is attenuated by dust and reradiated in the IR. Figure 13 shows that there is no trend in $\text{SFR}_{\text{total}}/\text{SFR}_{\text{UV}}$ as a function of $\xi(i_{775}, H_{160})$. Galaxies with high $\xi(i_{775}, H_{160})$ span the entire range of $\text{SFR}_{\text{total}}/\text{SFR}_{\text{UV}}$.

Taken together, this is evidence that spatial variations of dust are not the main driver of the ICD, and as such, the ICD requires spatial variations in stellar population ages in galaxies (perhaps with contributions from spatial variations in dust attenuation). This agrees with the conclusions from Papovich

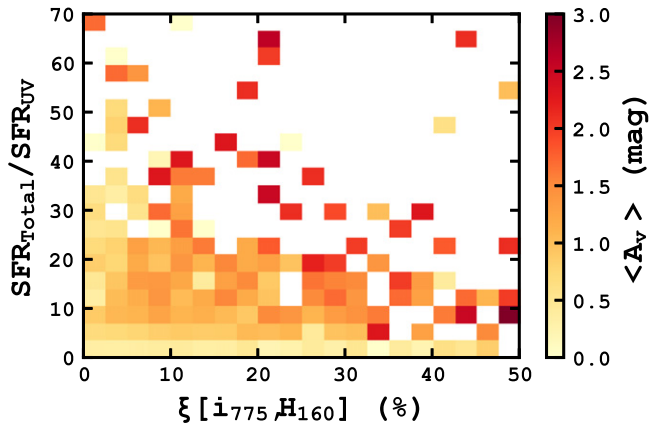


Figure 13. Ratio of the total SFR to the SFR derived from observed UV luminosity, $SFR_{\text{Total}}/SFR_{\text{UV}}$, as a function of ICD. The colored boxes show the average attenuation value (A_V) of the points within the region. Galaxies with IR-dominated SFRs have smaller ICDs than those with a lower $SFR_{\text{Total}}/SFR_{\text{UV}}$. At fixed $SFR_{\text{Total}}/SFR_{\text{UV}}$, there is a large spread in derived attenuation. This suggests that a mix of stellar population ages drives the ICD and attenuation plays a minor role.

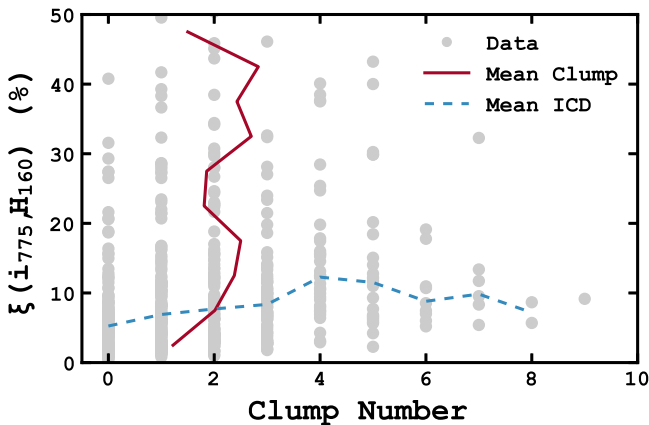


Figure 14. ICD as a function of number of clumps. The gray points are the individual galaxies. The red solid and blue dashed lines represent the average clump number in ICD bins and the average ICD value for different numbers of clumps, respectively.

et al. (2003, 2005) and Bond et al. (2011). Both groups acknowledge that extinction variations could play a role in providing variations in the blue starlight, but conclude that the effect is smaller than those produced by variations in segregated stellar populations of different mass-weighted ages. The ICD appears to be driven mostly by variations in the ages of stellar populations in galaxies.

5.6. Star-forming Clumps

Papovich et al. (2005) suggest that in order to have $ICD > 10\%$, young star-forming disk in galaxies are required to have a surrounding older spheroid; for higher ICDs ($> 20\% - 25\%$), they suggest that compact star-forming H II regions (discrete star-forming regions or clumps) are also required. This picture is corroborated in a recent study by Wuyts et al. (2012), who found that star-forming galaxies at $z \sim 2$, with stellar masses $\log(M/M_{\odot}) > 10$, have redder centers and bluer outer regions.

Figure 14 shows $\xi(i_{775}, H_{160})$ as a function of the number of clumps, using the catalog of Guo et al. (2014); see Section 2.8. The average $\xi(i_{775}, H_{160})$ value steadily increases for increasing

number of clumps but turns over after a galaxy contains at least four clumps. The average number of clumps for a given $\xi(i_{775}, H_{160})$ value shows a similar increase with increasing $\xi(i_{775}, H_{160})$ but does not show a turnover. For galaxies with low ($< 5\%$) ICD values, the mean number of clumps per galaxy is 1.2; for galaxies with higher ICDs ($> 5\%$), the mean number of clumps is 2.1. Therefore, we find that if a galaxy has at least two clumps, on average, it will have a high $\xi(i_{775}, H_{160})$ value. This trend continues, where galaxies with four or more clumps show median ICD of $> 10\%$. Therefore, the ICD is sensitive to the number of star-forming clumps.

The clump catalog provides several clump detection levels (see Section 2.8). When we increase the detection threshold (UV luminosity $> 5\%$ instead of 1%), we find that the mean number of clumps remains roughly constant (1–2) regardless of the $\xi(i_{775}, H_{160})$ value. Also, while the total number of clumps per galaxy is reduced, we find that the $\xi(i_{775}, H_{160})$ of galaxies with fewer than two clumps remains generally unchanged between the two UV luminosity thresholds.

Because the star-forming clumps are expected to form in gas-rich disks (e.g., Keres et al. 2005; Dekel & Birnboim 2006; Dekel et al. 2009a; Dekel & Burkert 2014), the ICD must trace galaxies that have a redder but still gaseous stellar disk. These individual clumps are thought to be relatively short lived (only 100 – 200 Myr; Wuyts et al. 2012), which would correspond well with the lifetimes of hot, blue stars contributing to the UV light associated with high ICD.

6. ON BULGES, CLUMPS, AND THE ICD

For the galaxies in this study, we find that as both the stellar mass and Sérsic index increase, the ICD decreases (Figure 5). This is unsurprising as previous studies suggest that galaxies with high Sérsic indices have smooth light profiles with little color variation across them (e.g., Daddi et al. 2004; van Dokkum et al. 2004; Szomoru et al. 2010), and these stellar populations produce little color dispersion as any variation is small relative to the total galaxy flux (Papovich et al. 2005).

However, the galaxies with high ICD values have intermediate stellar mass and are disk dominated ($n < 2$). As mentioned previously, Papovich et al. (2005) found that for a galaxy to have high ICD, a red bulge surrounded by a blue disk with H II regions (i.e., clumps) is required. Because high ICD is most prominent in disk-dominated morphologies and associated with star-forming clumps, the ICD is less sensitive to the red bulge component and more driven by the color variation between the underlying stellar disk and highly star-forming clump. We see this in the previous comparison of the $\xi(i_{775}, H_{160})$ computed with and without the central region (see Section 5.3), where we found that galaxies with their nuclear region removed show an increased $\xi(i_{775}, H_{160})$ (Figure 10).

Interpreted another way, the decrease of $\xi(i_{775}, H_{160})$ with increasing Sérsic index suggests that there is a continual suppression of the mechanism that causes high ICD (perhaps clumps) with spheroid formation. This shows that if galaxies are to form quiescent bulges or spheroids along with a star-forming disk or clumps (as is typical of classical Hubble sequence galaxies), it is only happening at this moderate ($10 < \log(M/M_{\odot}) < 11$) stellar mass range and with relatively small bulge contributions. Once a bulge contributes significantly to the galaxy’s morphology, the amount of ICD decreases dramatically, suggesting that the bulge plays a role in the homogenization of the galaxy’s stellar populations.

Two different effects could be associated with the formation of a bulge and subsequent reduction in the observed ICD. One theory is the “morphological quenching” (Martig et al. 2009) concept, by which the formation of the bulge stabilizes the gaseous disk against further fracturing and star formation. The second could be some feedback process associated with the bulge that removes any remaining gas from the disk, preventing new clump formation.

The first step in the quenching process is to form a strong bulge component. One scenario for this process is for clumps to migrate through dynamical friction to coalesce in the nuclei, and merge to form a bulge (e.g., Elmegreen et al. 2008; Dekel et al. 2009a, 2009b; Ceverino et al. 2010). The galaxies with high ICD values also show negative color gradients (Figure 9), suggesting that the central stars are older (or perhaps more attenuated by dust) than the outer star-forming regions. Other studies (e.g., Guo et al. 2012; Wuyts et al. 2012, 2013; Adamo et al. 2013) find that central clumps are both older (by $\gtrsim 500$ Myr) and more attenuated than the clumps in the outskirts, suggesting that migration plays a significant role.

Of course, not all galaxies in the moderate stellar mass range have high ICD values. Either only some galaxies have periods of high ICD, or all galaxies go through such a phase, but the period of elevated ICD is very short lived. If all galaxies experience a period of elevated ICD at some point during their evolution, then the characteristic timescale of high ICD is the product of the time spanned by the look-back time across the redshift range (2.4 Gyr) and the fraction of sources with high ICD. In this work, 21% of galaxies have $\xi(i_{775}, H_{160}) > 10\%$. Therefore, if all galaxies go through a high ICD phase, then the timescale of high ICD is approximately 375 Myr. This timescale is similar to the predicted clump survival timescale of 200–250 Myr (Wuyts et al. 2012).

Regardless of the mechanism at work, there is a distinct suppression in the ICD of galaxies once a bulge is formed. Galaxies that contain highly star-forming clumps match well the description of these high ICD objects, and clump migration could be a primary cause of ICD suppression. It will take further investigation in the future to better associate galaxies showing high ICD with star-forming clumps.

7. SUMMARY

In this work, we investigate the dependence of the rest-frame UV and optical ICD on other galaxy properties. We define the ICD as the ratio of the square difference of the image flux-intensity values about the mean galaxy color to the square of the total image flux. It is a measure of the amount of variation in the stellar diversity of a galaxy, that is, separated red and blue stellar populations. Using imaging from CANDELS of GOODS-S and the HUDF, we select galaxies between $1.5 < z < 3.5$, an H_{160} magnitude brighter than 25 mag, and a requirement that the S/N be sufficient enough to provide an accurate measurement of the ICD (see Section 2.3). This selection yields 2601 galaxies.

We present our results from comparing the ICD to the stellar mass of the galaxies (Section 4.1), the morphology based on Sérsic index (Section 4.2), and SFRs (Section 4.3). We then investigate possible causes of the ICD, including mergers (Section 5.1), physical size (Section 5.2), color gradients (Section 5.3), bandpass shifting effects (Section 5.4), attenuation (Section 5.5), and clumpy star-forming regions (Section 5.6). We attribute ICD to heterogeneous stellar populations

(possibly clumps) with a possible contribution from dust attenuation.

The major results of this work, with accompanying interpretations, are as follows:

1. Galaxies have the largest amount of stellar population diversity, as measured by the ICD, at stellar masses $10 < \log(M/M_{\odot}) < 11$. This stellar mass range corresponds well to the range in which local galaxies experience a decrease in their star formation efficiency, and galaxies at $z \sim 2$ that are found to show star-forming clumps. Therefore, the stellar population diversity driving the ICD could be discrete, highly star-forming regions contrasted against an older, redder, underlying population.
2. High ICD is preferentially found in galaxies with extended light profiles (Sérsic index < 2). This suggests that galaxies only have diverse stellar populations when there is little or no bulge present.
3. There is a continual suppression in the mechanism that causes high ICD with increasing Sérsic index. This could be due to formation of clumps, which initially increase the ICD and then migrate toward the center and coalesce into a quiescent bulge. The presence of this bulge then stabilizes the disk against fragmentation and new clump formation, which suppresses the ICD.

The results suggest that some fraction of galaxies with high ICD are a result of the combination of structures such as quiescent bulges and star-forming (perhaps clump) disks in galaxies. If this corresponds to the formation of the spiral galaxies indicative of the Hubble sequence, then this phase occurs only in galaxies with stellar masses $10 < \log(M/M_{\odot}) < 11$ and when the bulge component remains relatively small ($n < 2$).

The authors also wish to thank the anonymous referee whose comments and suggestions significantly improved both the quality and clarity of this work. This work is based on observations taken by the CANDELS Multi-Cycle Treasury Program with the NASA/ESA *HST*, which is operated by the Association of Universities for Research in Astronomy, Inc., under NASA contract NAS5-26555. We also make use of partial support from NSF AST-0808133. We utilize the Rainbow Cosmological Surveys Database, which is operated by the Universidad Complutense de Madrid (UCM), partnered with the University of California Observatories at Santa Cruz (UCO/Lick, UCSC). Several open source resources are used to complete this study: Python (van Rossum & de Boer 1991), along with Matplotlib (Hunter 2007) and IPython (Perez & Granger 2007).

REFERENCES

- Abraham, R. G., Nair, P., McCarthy, P. J., et al. 2007, *ApJ*, 669, 184
 Adamo, A., Östlin, G., Bastian, N., et al. 2013, *ApJ*, 766, 105
 Arnouts, S., Cristiani, S., Moscardini, L., et al. 1999, *MNRAS*, 310, 540
 Baldry, I. K., Glazebrook, K., Brinkmann, J., et al. 2004, *ApJ*, 600, 681
 Beckwith, S. V. W., Stiavelli, M., Koekemoer, A. M., et al. 2006, *AJ*, 132, 1729
 Bell, E. F., van der Wel, A., Papovich, C., et al. 2012, *ApJ*, 753, 167
 Bertin, E., & Arnouts, S. 1996, *A&AS*, 117, 393
 Blanton, M. R., Dalcanton, J., Eisenstein, D., et al. 2001, *AJ*, 121, 2358
 Blanton, M. R., Hogg, D. W., Bahcall, N. A., et al. 2003, *ApJ*, 594, 186
 Bolzonella, M., Miralles, J.-M., & Pelló, R. 2000, *A&A*, 363, 476
 Bond, N. A., Gawiser, E., & Koekemoer, A. M. 2011, *ApJ*, 729, 48
 Bouwens, R. J., Illingworth, G. D., Oesch, P. A., et al. 2010, *ApJL*, 708, L69

- Brammer, G. B., van Dokkum, P. G., & Coppi, P. 2008, *ApJ*, 686, 1503
- Bruzual, G., & Charlot, S. 2003, *MNRAS*, 344, 1000
- Calzetti, D., Armus, L., Bohlin, R. C., et al. 2000, *ApJ*, 533, 682
- Ceverino, D., Dekel, A., & Bournaud, F. 2010, *MNRAS*, 404, 2151
- Ceverino, D., Dekel, A., Tweed, D., & Primack, J. 2015, *MNRAS*, 447, 3291
- Chabrier, G. 2003, *PASP*, 115, 763
- Conselice, C. J., Grogan, N. A., Jogee, S., et al. 2004, *ApJL*, 600, L139
- Daddi, E., Cimatti, A., Renzini, A., et al. 2004, *ApJ*, 617, 746
- Daddi, E., Dickinson, M., Morrison, G., et al. 2007, *ApJ*, 670, 156
- Dahlen, T., Mobasher, B., Faber, S. M., et al. 2013, *ApJ*, 775, 93
- de Vaucouleurs, G. 1948, *AnAp*, 11, 247
- Dekel, A., & Birnboim, Y. 2006, *MNRAS*, 368, 2
- Dekel, A., Birnboim, Y., Engel, G., et al. 2009a, *Natur*, 457, 451
- Dekel, A., Sari, R., & Ceverino, D. 2009b, *ApJ*, 703, 785
- Dekel, A., & Burkert, A. 2014, *MNRAS*, 438, 1870
- Dickinson, M. 2000, *RSPTA*, 358, 2001
- Dickinson, M., Papovich, C., Ferguson, H. C., & Budavari, T. 2003, *ApJ*, 587, 25
- Dutton, A. A. 2009, *MNRAS*, 396, 121
- Ellis, R. S., McLure, R. J., Dunlop, J. S., et al. 2013, *ApJL*, 763, L7
- Elmegreen, B. G., Bournaud, F., & Elmegreen, D. M. 2008, *ApJ*, 688, 67
- Elmegreen, B. G., Elmegreen, D. M., Fernandez, M. X., & Lemonias, J. J. 2009a, *ApJ*, 692, 12
- Elmegreen, D. M., Elmegreen, B. G., Marcus, M. T., et al. 2009b, *ApJ*, 701, 306
- Elmegreen, D. M., Elmegreen, B. G., Rubin, D. S., & Schaffer, M. A. 2005, *ApJ*, 631, 85
- Förster Schreiber, N. M., Shapley, A. E., Genzel, R., et al. 2011, *ApJ*, 739, 45
- Franx, M., van Dokkum, P. G., Schreiber, N. M. F., et al. 2008, *ApJ*, 688, 770
- Giavalisco, M., Ferguson, H. C., Koekemoer, A. M., et al. 2004, *ApJL*, 600, L93
- Giavalisco, M., Steidel, C. C., & Macchetto, F. D. 1996, *ApJ*, 470, 189
- Grogan, N. A., Kocevski, D. D., Faber, S. M., et al. 2011, *ApJS*, 197, 35
- Grützbauch, R., Chuter, R. W., Conselice, C. J., et al. 2011, *MNRAS*, 412, 2361
- Guo, Y., Ferguson, H. C., Bell, E. F., et al. 2014, arXiv:1410.7398, 22
- Guo, Y., Ferguson, H. C., Giavalisco, M., et al. 2013, *ApJS*, 207, 24
- Guo, Y., Giavalisco, M., Ferguson, H. C., Cassata, P., & Koekemoer, A. M. 2012, *ApJ*, 757, 120
- Hunter, J. D. 2007, *CSE*, 9, 90
- Ilbert, O., Arnouts, S., McCracken, H. J., et al. 2006, *A&A*, 457, 841
- Kauffmann, G., Heckman, T. M., White, S. D. M., et al. 2003, *MNRAS*, 341, 54
- Kennicutt, R. C. 1998, *ARA&A*, 36, 189
- Keres, D., Katz, N., Weinberg, D. H., & Dave, R. 2005, *MNRAS*, 363, 2
- Koekemoer, A. M., Faber, S. M., Ferguson, H. C., et al. 2011, *ApJS*, 197, 36
- Kriek, M., van Dokkum, P. G., Labbé, I., et al. 2009, *ApJ*, 700, 221
- Laidler, V. G., Grogan, N., Clubb, K., et al. 2006, in ASP Conf. Ser. 351, *Astronomical Data Analysis Software and Systems XV*, ed. C. Gabriel, C. Arviset, D. Ponz, & S. Enrique (San Francisco, CA: ASP), 351
- Law, D. R., Steidel, C. C., Erb, D. K., et al. 2007, *ApJ*, 656, 1
- Law, D. R., Steidel, C. C., Shapley, A. E., et al. 2012, *ApJ*, 745, 85
- Lee, B., Giavalisco, M., Williams, C. C., et al. 2013, *ApJ*, 774, 47
- Lotz, J. M., Davis, M., Faber, S. M., et al. 2008, *ApJ*, 672, 177
- Lotz, J. M., Primack, J., & Madau, P. 2004, *AJ*, 128, 163
- Lowenthal, J. D., Koo, D. C., Guzman, R., et al. 1997, *ApJ*, 481, 673
- Magdis, G. E., Rigopoulou, D., Huang, J.-S., & Fazio, G. G. 2010, *MNRAS*, 401, 1521
- Martig, M., Bournaud, F., Teyssier, R., & Dekel, A. 2009, *ApJ*, 707, 250
- Oesch, P. A., Bouwens, R. J., Illingworth, G. D., et al. 2010, *ApJL*, 709, L16
- Oke, J. B. 1974, *ApJS*, 27, 21
- Papovich, C., Dickinson, M., & Ferguson, H. C. 2001, *ApJ*, 559, 620
- Papovich, C., Dickinson, M., Giavalisco, M., Conselice, C. J., & Ferguson, H. C. 2005, *ApJ*, 631, 101
- Papovich, C., Giavalisco, M., Dickinson, M., Conselice, C. J., & Ferguson, H. C. 2003, *ApJ*, 598, 827
- Papovich, C., Labbé, I., Quadri, R. F., et al. 2014, arXiv:1412.3806
- Peng, C. Y., Ho, L. C., Impey, C. D., & Rix, H.-W. 2002, *AJ*, 124, 266
- Perez, F., & Granger, B. E. 2007, *CSE*, 9, 21
- Salmon, B., Papovich, C., Finkelstein, S. L., et al. 2014, arXiv:1407.6012
- Salpeter, E. E. 1955, *ApJ*, 121, 161
- Sérsic, J. L. 1963, *BAAA*, 6, 41
- Speagle, J. S., Steinhardt, C. L., Capak, P. L., & Silverman, J. D. 2014, *ApJS*, 214, 15
- Szomoru, D., Franx, M., Bouwens, R. J., et al. 2011, *ApJL*, 735, L22
- Szomoru, D., Franx, M., van Dokkum, P. G., et al. 2010, *ApJL*, 714, L244
- van der Wel, A., Bell, E. F., Häussler, B., et al. 2012, *ApJS*, 203, 24
- van Dokkum, P. G., Franx, M., Förster Schreiber, N. M., et al. 2004, *ApJ*, 611, 703
- van Rossum, G., & de Boer, J. 1991, *CWI Quarterly*, 4, 283
- Wang, T., Huang, J.-S., Faber, S. M., et al. 2012, *ApJ*, 752, 134
- Williams, R. J., Quadri, R. F., Franx, M., et al. 2010, *ApJ*, 713, 738
- Windhorst, R. A., Cohen, S. H., Hathi, N. P., et al. 2011, *ApJS*, 193, 27
- Wuyts, S., Förster Schreiber, N. M., Lutz, D., et al. 2011a, *ApJ*, 738, 106
- Wuyts, S., Förster Schreiber, N. M., Genzel, R., et al. 2012, *ApJ*, 753, 114
- Wuyts, S., Förster Schreiber, N. M., Nelson, E. J., et al. 2013, *ApJ*, 779, 135
- Wuyts, S., Förster Schreiber, N. M., van der Wel, A., et al. 2011b, *ApJ*, 742, 96
- Zibetti, S., Gallazzi, A., Charlot, S., Pierini, D., & Pasquali, A. 2012, *MNRAS*, 428, 1479